Fractality and growth of He bubbles in metals

Shin Kajita

*Institute of Materials and Systems for Sustainability, Nagoya University, Nagoya 464-8603, Japan**

Atsushi M. Ito

National Institute for Fusion Science, 322-6, Oroshi-cho, Toki 509-5292, Japan

Department of Fusion Science, The Graduate University for Advanced Studies (SOKENDAI), 322-6 Oroshi-cho, Toki 509-5292, Japan

Noriyasu Ohno

Graduate School of Engineering, Nagoya University, Nagoya 464-8603, Japan

(Dated: March 29, 2017)

Abstract

Pinholes are formed on surfaces of metals by the exposure to helium plasmas, and they are regarded as the initial process of the growth of fuzzy nanostructures. In this study, number density of the pinholes is investigated in detail from the scanning electron microscope (SEM) micrographs of tungsten and tantalum exposed to the helium plasmas. A power law relation was identified between the number density and the size of pinholes. From the slope and the region where the power law was satisfied, the fractal dimension D and $s_{\min}$, which characterize the SEM images, are deduced. Parametric dependences and material dependence of D and $s_{\min}$ are revealed. To explain the fractality, simple Monte-Carlo simulations including random walks of He atoms and absorption on bubble was introduced. It is shown that the initial position of the random walk is one of the key factors to deduce the fractality. The results indicated that new nucleations of bubbles are necessary to reproduce the number-density distribution of bubbles.

PACS numbers:

*Electronic address: kajita.shin@nagoya-u.jp

I. INTRODUCTION

Helium (He) plasma irradiation leads to fuzzy nanostructures on metallic surfaces [1–4]. From experiments, it was suggested that the growth and migration of He bubbles are deeply related with the formation of the nanostructures [5, 6]. To understand the mechanism of the growth of the nanostructures in more detailed manner, various theoretical and simulation works have been conducted [7–17]. For ex., the nucleation of the helium bubble in tungsten materials had been researched by using calculations based on density functional theory (DFT) [11, 12, 18–20]. The DFT researches clarified that helium atoms easily nucleate in tungsten materials. The growth to larger bubbles from a nuclei had also been simulated by using molecular dynamics (MD) [15, 21–25].

To confirm the physics involved, it is of importance to compare quantitatively between theoretical studies and experiments with some indices. Comparisons were made on the surface pinhole densities and sizes [7], the temperature ranges of nanostructure growth condition [9], and the nanostructured layer thickness [16]. One of the methods to quantify the morphology changes is the fractal analysis. It was found that the nanostructures have fractality in various point of view [26, 27]: the surface morphology, the relations between the porosity and height, and pinhole number and sizes. Concerning the pinholes on the surfaces, which should reflect the bubbles formed in the metals, it is of interest to investigate because they are highly likely to play crucial roles on morphology changes.

In this study, focusing on pinholes formed on the surface by the exposure to the He plasmas, the size distribution of the pinholes formed on tungsten (W) and tantalum (Ta) samples are investigated in detail using scanning electron microscope (SEM) micrographs observed from the top. It is shown that a power law relation can be identified between the cumulative number of pinholes formed on the surface and its sizes and that they varied with the He fluence, the surface temperature, and so on.

To demonstrate the fractality identified on the size of bubbles, simple Monte-Carlo (MC) models are introduced to model the growth of He bubbles on metals. Until now, the number-size relation of He bubbles has been discussed using the MD simulation [24], which can directly observe the growth process and the emission of loop punching. However, by the limitation of space and time scales due to computer resources, the sample number of helium bubbles is insufficient to discuss the fractal structure in the MD. Although the kinetic Monte-

Carlo (KMC) [28] and objective KMC [29] can probably treat the sufficient space and time scales, simpler models may be better to investigate the origin of the fractality identified. In Sec. II, after explaining analysis method, experimental observations on W and Ta surfaces are shown. In Sec. III, two MC simulation models are introduced. Based on comparisons of simulation results, we will discuss key processes to exhibit the fractality.

II. EXPERIMENTAL OBSERVATION

A. Method

Figure 1(a) show an SEM micrographs of the He irradiated sample with the contrast profile. The sample is a single crystal (SC) W with the crystal orientation of {100}. The sample was exposed to the He plasma in the divertor simulator NAGDIS-II (Nagoya Divertor Simulator) at the incident ion energy of 55 eV at the surface temperature of 1800 K up to the He fluence of 1.8×10^{25} m^{-2}. In Table I, the samples and the irradiation conditions used for the analysis are summarized, and W2 is the sample used in Fig. 1. In addition to SC-W, polycrystalline (PC) W sample was used. Major important parameters, i.e., the surface temperature, the incident ion energy, and the He fluence are shown in Table I. In the contrast profile in Fig. 1(a), we can see that there is a peak in the contrast level around 120-130. In Fig. 1(b), three digitized images with the threshold level of 40, 60, and 80 are shown. All the three cases are in the left wing (bright side) of the contrast distribution and only pinholes are counted as black pixels.

Figure 1(c) shows the cumulative number density distribution of pinholes as a function of the hole area measured from the digitized images. From the double logarithmic plot, it can be identified that the relation between the number density of pinholes, N, and the hole area, S, satisfied the power law relation, namely,

$$N \propto S^{-D/2}. \tag{1}$$

Here, the value D corresponds to the steepness of the slope, and the factor of two below D in Eq. (1) was used to discuss the relation between the number density and the characteristic length of the hole, typically the diameter. The number of the black dots, consequently, D increased with increasing the contrast threshold. This is probably because the influence of the threshold would be more sensitive for smaller holes. In this image, we think that

the threshold of 80 was too high and better to eliminate the influence of the noises on the images by decreasing the threshold from 1.57±0.08 at the threshold of 40 to 1.89±0.05 at 80, because it was identified in some location that two pinholes connected and changed the profile. Here, the error represented a fitting error obtained in the fitting process. Although the threshold should depend on the brightness of the image, we usually use the threshold lower than 50. We should admit that the value D obtained from this method using SEM images have some inevitable ambiguity caused from the contrast, typically less than ±10%.

In addition to the slope D, another important parameters for the analysis the minimum area where the power law is satisfied, $s_{\min}$. From Fig. 1(c), for ex., $s_{\min}$ can be obtained from the knee of the slope, roughly, 10^4 nm^2.

B. Tungsten

Figures 2(a-1)-(a-3) show SEM micrographs of the sample W4. It is known that there is a threshold in the incident ion energy for the formation of the nanostructures around 20-30 eV [6]. Because the incident ion energy of W4 was on the border of the threshold, the fiberform structure did not grow on the surface, though the He fluence was much higher than recognized necessary fluence of 5×10^{25} m^{-2}. The grain orientation was determined by an orientation imaging microscope (OIM) [30].

The analysis was conducted for surfaces with the crystal orientation of {001}, {113}, and {407}. The profile slightly altered with changing the crystal orientation. On {113} surface, the obtained D was 2.63±0.10, and $s_{\min}$ was estimated to be 4.2×10^2 nm^2. On {001} surface, the number density slightly increased at $S \sim 10^3$ nm^2, and the slope decreased compared with the {113} surface. Approximately, variation in D by crystal orientation was 20%.

Figures 3(a-1)-(a-3) show SEM micrographs of W1-W3, respectively, and the relations between the hole density and the hole area are shown in Fig. 3(b). It is seen that D and $s_{\min}$ both increased with the He fluence: from 1.46 ± 0.18 to 2.29 ± 0.14 for D and from 2.4×10^2 to 1.4×10^3 nm^2 for $s_{\min}$.

They are not only dependent on the He fluence, but on other parameters as well such as the irradiated surface temperature. Figures 4(a-1)-(a-2) show SEM micrographs of W1 and W5, respectively, and Fig. 4(b) shows the cumulative number density distribution of pinholes as a function of the pinhole area. The irradiation temperature of W1 and W5 was 1800 and

1200 K, respectively. Although the fluence of W5 was twice lower compared with that of W5, the temperature dependence clearly appeared on the number density distribution, as shown in Fig. 4(b). It is identified that the obtained D decreases and $s_{\min}$ increases with the surface temperature.

In Figs. 5(a) and (b), the obtained D and $s_{\min}$, respectively, are summarized as a function of the He fluence. Although the relation was not so simple, because the obtained values also have dependences on the surface temperature and the incident ion energy, both of D and $s_{\min}$ increased with the He fluence up to $\sim 5\times10^{25}$ m^{-2}. When the incident ion energy was on the boundary of the energy threshold of 20-30 eV, $s_{\min}$ was clearly lower than the higher energy cases. When the temperature is lower, say 1200 K, D is higher than the other low He fluence cases.

C. Tantalum

Table II shows the irradiation conditions of tantalum samples (Ta1-Ta5) used for the analysis. The temperature range was 940 to 1480 K, and the fluence was higher than 10^{25} m^{-2} on all the samples. Pinholes were formed after the He plasma irradiation when the surface temperature was higher than 800 K, and, also, fuzzy tantalum was formed when the surface temperature was 1100 K and the He fluence was greater than 10^{26} m^{-2} [31]. Pore density distribution has been analyzed previously on Ta surfaces exposed to the He plasmas [32]. It was found that small pores and large pores decrease and increase, respectively, with the temperature.

Figures 6(a) and (b) shows the cumulative number density distribution of pinholes on Ta2 and Ta4, respectively, as a function of the area of pinholes. Note that the scales of the vertical and horizontal axis are different in Figs. 6(a) and (b). SEM micrographs of the samples are shown in the insets. It is seen that the pinholes are formed on the surface, and the sizes of the pinholes are quite different between the cases at 1090 and 1420 K. In both cases, power law relation can be identified in some scale; it deviated when the scale is small, i.e., 2-300 nm^2 at 1090 K and 5×10^3 nm^2 at 1420 K. Such a deviation was not identified on W samples. This may be because of noises of the SEM images due to short time image scan for Ta cases. We omit the deviation and focused on D and $s_{\min}$ for tantalum as well. From the number density distribution, $D = 1.89 \pm 0.10$ and $s_{\min} = 6.4 \times 10^3$ nm^2 at 1090 K, and

$D = 0.82 \pm 0.13$ and $s_{\min} = 1.8 \times 10^4$ nm^2 at 1420 K.

Figures 7(a) and (d) show the temperature dependences of D and $s_{\min}$, respectively. In Ta case, because the fluence and incident ion energy dependences are not so significant in the ranges in table II, the dependence can be well explained as a function of the temperature. With increasing the surface temperature from 940 to 1480 K , D decreased from two to unity, while $s_{\min}$ increased up to $\sim 2 \times 10^5$ nm^2. It is interesting to compare D and $s_{\min}$ between Ta and W. In case of W, D increased up to 2.5 and $s_{\min}$ is comparable or less than 1×10^4 nm^2 under the conditions where the nanostructures are formed. Fuzzy Ta nanostructures were formed on the surface when the surface temperature was 1100 K, where $s_{\min}$ is 1×10^4 nm^2, as can be seen in Fig. 7. It is likely that D and $s_{\min}$ can be measures to identify proper condition of the formation of nanostructures.

D. Discussion

Fractality in the number-size distribution has been identified on various places [33]. Typical examples are on the craters of planets [34] or crater ejecta on Venus [35]. Concerning the craters on the moon, they have fractality between the size and the number with D of ~ 2.0 [34]. It was identified that the fractality on the craters was originated from the size distribution of meteorites. To support the number-size distribution of meteorites, experimental demonstration has been conducted to destruct basaltic bodies by high velocity impact [36]; interestingly, fractality in the number-size distribution has been found on fragments. It was identified in general that fragmentation processes such as weathering, explosions, and impacts often produce a fractal distribution over a wide range of scales [33].

The number density distribution of pinholes reflects that of He bubbles beneath the surface. Concerning the He bubbles, the distribution was determined not by fragmentation but by coalescence process. In the next section, we discuss the mechanism of the fractality identified on the coalescence processes based on a Monte Carlo simulation.

III. SIMULATION

A. Model

From experiments, it was confirmed that the size distribution of He bubble pinhole satisfied the power law relation. The power law relation indicates that the size distribution of the He bubbles has a fractal structure. To discuss the origin of the fractality, two different simple Monte-Carlo models are proposed in the present work.

The first model is composed of the random walk of He atoms and the growth of He bubbles due to absorption of the helium atoms. A simulation box is set in a two dimensional (x, z) space. The widths of the simulation box in x and z directions are w and h, respectively. The four sides of the simulation box connect to the opposite side under the periodic boundary condition. In this simulation box, the following random walk cycles are performed. A He atom is put in the simulation box. The initial position of the He atom is decided by uniform random distribution. Then, the He atom moves to the four adjacent cells, i.e., the left, right, up, or down, at random. The distance of the movement at a step is simply unity. The movement of the He atom is repeated N_{walk} steps. If the He atom reaches a He bubble, the He atom is absorbed on the He bubble, and the size is incremented. Here, the size of a He bubble is determined by the number of He atoms included in the bubble, n. The radius of a He bubble, r, is defined as a square root of n, namely, $r = \sqrt{n}$, based on the fact that the radius is determined from a spherical equilibrium bubble. By an absorption process, the number of He atoms included in the bubble increased from n to $n + 1$. On the other hand, if the He atom did not encounter any He bubbles during the movements of N_{walk} steps, it is regarded as a nucleation, and, then, a new He bubble whose size is unity is generated on the final position of the He atom. The number of the random walk steps, N_{walk}, is likely to relate to the diffusivity. On the other hand, the number of the above cycles, N_{step}, corresponds to the He fluence. In the present calculation, the parameters are set to $w = h = 1000$ and $N_{\mathrm{walk}} = 1000$. Figure 8(a) shows a schematic of random walk processes in the simulation. The He atom started from 'A' was absorbed by the helium bubble 'C', while the He atom started from 'B' was not absorbed during N_{walk} steps, and, then, a new He bubble is generated in the final position 'D'.

The second model introduced a surface effect; the periodic boundary condition is adopted

in the x-direction, and the top boundary at $z = 0$ is regarded as a surface. There is no limit in the bottom of the box in z-direction, i.e., $h = \infty$. He atoms are injected from the surface side perpendicularly. The initial position of He atoms in x-direction is determined at random, while that in z-direction is fixed at the depth of d from the surface. However, if bubbles existed at $< d$, the initial position is shifted to deeper so that the total penetration depth, i.e., the distance in which helium atom passes through the material region, corresponds to d. The sole difference between the first and second models is in the initial position in z direction. The rules of the random walk, the absorption, and the nucleation in the second model are the same as those in the first model. Furthermore, the second model is similar to the Monte-Carlo part of the previous MD-MC hybrid simulation [17, 37], in which an early phase of W fuzzy nanostructure formation has been successfully reproduced. In the second model, d is set to 100, and the other parameters are the same as the calculation of the first model.

Figure 8(b) shows a schematic illustrating the injection process in this model. The solid and dashed lines are trajectories of injected He atoms. In the second model, the length of the dashed lines, i.e., inside bubbles, are not counted as the injection depth d. The rhombuses 'E', 'F', and 'G' are start positions of random walks. The He atom injected into the position 'E' pass through material all the way, while the He atoms injected to the positions 'F' and 'G' pass through He bubbles. The penetration length through material is always d. That is, $d = d_1 + d_2 = d_3 + d_4$.

B. Results and discussion

Figure 9(a-1)-(a-3) shows the time evolution of the spatial distribution of He bubbles in the first model at $N_{\mathrm{step}} = 10^5$, 4×10^5, and 7×10^5. The size of He bubbles increases with the elapsed time. The space distribution of the He bubbles was kept roughly uniform. Figure 10(a) shows the cumulative number density distributions of bubbles in the first model at $N_{\mathrm{step}} = 10^5$ and 10^6. It is seen that the distribution does not follow the power law scaling. The number of small helium bubbles is significantly low, while many large bubbles are formed. It should be said that the power law scaling in the number-size distribution of He bubbles could not be reproduced in the first model.

Figure 9(b-1)-(b-3) shows the time evolution of the spatial distribution of He bubbles in

the second model at $N_{\rm step} = 10^5$, 4×10^5, and 7×10^5. It is observed that the bubble formed region is gradually extended to deeper. Moreover, the size of He bubbles decreases with the depth. Figure 10(b) is the cumulative number density distributions of bubbles in the second model at $N_{\rm step} = 10^5$ and 10^6. The size distribution satisfied the power law scaling both at $N_{\rm step} = 10^5$ and 10^6. From the comparison with the first model, it is suggested that the surface effect introduced in the second model is a key to cause the fractal feature in the number-density relation of He bubbles.

The failure of the first model is in the fact that the grown bubbles gradually fill the simulation box. Consequently, almost all the injected He atoms are trapped by the bubbles, and new nucleation rarely occurs. It is noted that we quickly checked whether the distribution alters when using a three dimensional model, and found that the similar distribution was obtained even if the three dimensional effect was taken into consideration. On the other hand, in the second model, new nucleation constantly occurs in the deeper region while bubbles are grown at the same time. It is likely that self-similarity appeared in the number-size distribution is attributed to the fact that the nucleation and the growth in size occur continuously without changing the rates significantly.

Here, let us think about the processes controlling the size distribution. Considering the density of bubbles with n atoms, $N(n)$, a following simple rate equation would be satisfied in the present model

$$\frac{dN(n)}{dt} = a_{n-1}N(n-1) - a_n N(n), \tag{2}$$

where a_n is the absorption rate of He atoms to a He bubble with n atoms. When steady state assumption is satisfied, i.e. $dN(n)/dt = 0$, following relation is obtained:

$$N(n) = \frac{a_{n-1}}{a_n} N(n-1) \tag{3}$$

$$= a_1 N(1) \frac{1}{a_n}. \tag{4}$$

If the number-size distribution can be scaled in the power law with D, a_n can be written as

$$a_n \propto r^D. \tag{5}$$

In the present model, a_n should be proportional to the occupation area of a bubble, and $r = \sqrt{n}$; thus,

$$a_n \propto \pi r^2 \propto n. \tag{6}$$

In the present simulation, from the fact that the profile did not change so much at $n < 2\times10^2$, it can be said that the steady state approximation is valid for the small bubbles. Indeed, in Fig. 10(b), from $n = 1$ to 10^3, the density also changed almost by three orders of magnitudes, indicating that D was approximately two.

In experiments, D varied from 0.8 to 2.6; the value can be higher or lower than the deduced value from the simple simulation. In actuality, the absorption rate might be proportional to the volume of the bubble, the size of bubbles would not satisfy the relation $r \propto n$ especially when the temperature is high, and coalescences of bubbles and bursting of bubbles on the surface could change the number-size distribution. Those effects could change D. It is of interest to investigate the variation of D further with simulation by taking into account those effects.

IV. CONCLUSIONS

The size of pinholes formed on metal surfaces by helium plasma irradiation was investigated in detail using scanning electron microscope (SEM) micrographs. We digitized SEM images and counted the number and area of pinholes formed on tungsten and tantalum exposed to helium plasmas. A power law relation was identified between the number density and the size of pinholes, and two indices (D and $s_{\min}$) that characterize the images were deduced. We should admit that this method is slightly dependent on the contrast of the image and threshold of digitization, but the error is roughly $\pm10\%$ for D.

We analyzed pinholes formed on single crystal and polycrystalline tungsten surface. Concerning D, which corresponds to the slope of the relation between the number density and size of the pinholes, it has a clear dependence on the helium fluence in addition to the temperature when the nanostructure growth condition was satisfied. It increased from unity to 2.5 with changing the morphology up to the helium fluence of 5×10^{25} m^{-2}, which is the typical necessary helium fluence for full growth of the fuzzy nanostructures. We analyzed samples of which the sample temperature during the irradiation was in the range of 1200-1800 K. In this temperature range, $s_{\min}$ also increased with the He fluence and changed from 10^3 to 10^4 nm^2. As for tantalum, clear dependences of D and $s_{\min}$ were identified on the surface temperature. From 900 to 1500 K, D decreased from two to unity, and $s_{\min}$ increased from 10^3 to 10^5 nm^2. From the analogy to the case of tungsten, it was suggested

that around 1100 K is most plausible or similar conditions for the growth of fuzzy nanostructures on the surface. Indeed, it was revealed from experiments that the nanostructure growth was identified on the temperature range. Analysis of pinholes formed on the surface during the helium plasma irradiation can give indices to identify the formation condition of nanostructure growth.

Simple Monte-Carlo (MC) simulation was used to reproduce the fractality identified in the size-density distribution of He bubbles. He atoms are introduced in the simulation box, and random walks and absorption to He bubbles are taken into consideration. When the initial position was chosen randomly, small bubbles quickly disappeared because new nucleation did not occur sufficiently, and the power law relation was not realized. When the surface effects were taken into consideration to determine the initial positons, the power law relation was well reproduced. In the present simple model, the fractal dimension was approximately two. In future, it is of interest to conduct quantitative comparisons in D by taking into consideration the effects that were not introduced in this study: three dimensional effects, coalescences of He bubbles, bursting of He bubbles on the surface, and so on.

Acknowledgements

This work was supported in part by a Grant-in-Aid for Scientific Research (B) 15H04229 and 15H05563 from the Japan Society for the Promotion of Science (JSPS) and National Institute for Fusion Science (NIFS) collaborative research programs (NIFS15KOAH032 and NIFS16KNSS068). Numerical simulations were carried out by using the Plasma Simulator at NIFS and the HELIOS supercomputer system at the Computational Simulation Centre of International Fusion Energy Research Centre (IFERC-CSC), Aomori, Japan, under the Broader Approach collaboration between Euratom and Japan, implemented by Fusion for Energy and JAEA.

---

[1] S. Takamura, N. Ohno, D. Nishijima, and S. Kajita: Plasma Fusion Research **1** (2006) 051.

[2] G. De Temmerman, K. Bystrov, J. J. Zielinski, M. Balden, G. Matern, C. Arnas and L. Marot: Journal of Vacuum Science & Technology A **30** (2012) 041306.

[3] S. Kajita, T. Yoshida, D. Kitaoka, R. Etoh, M. Yajima, N. Ohno, H. Yoshida, N. Yoshida and Y. Terao: Journal of Applied Physics **113** (2013) 134301.

[4] S. Takamura and Y. Uesugi: Applied Surface Science **356** (2015) 888.

[5] M. Baldwin and R. Doerner: Nucl. Fusion **48** (2008) 035001 (5pp).

[6] S. Kajita, W. Sakaguchi, N. Ohno, N. Yoshida and T. Saeki: Nucl. Fusion **49** (2009) 095005.

[7] S. Sharafat, A. Takahashi, K. Nagasawa and N. Ghoniem: J. Nucl. Mater. **389** (2009) 203.

[8] Y. V. Martynenko and M. Y. Nagel: Plasma Physics Reports **38** (2012) 996.

[9] S. I. Krasheninnikov: Physica Scripta **2011** (2011) 014040.

[10] X.-C. Li, Y.-N. Liu, Y. Yu, G.-N. Luo, X. Shu and G.-H. Lu: Journal of Nuclear Materials **451** (2014) 356.

[11] A. Takayama, A. Ito, S. Saito, N. Ohno and H. Nakamura: Jpn. J. Appl. Phys. **52** (2013) 01AL03.

[12] T. Tamura, R. Kobayashi, S. Ogata and A. M. Ito: Modelling Simul. Mater. Sci. Eng. **22** (2014) 015002.

[13] S. Krasheninnikov, T. Faney and B. Wirth: Nuclear Fusion **54** (2014) 073019.

[14] R. Smirnov, S. Krasheninnikov and J. Guterl: Journal of Nuclear Materials **463** (2015) 359.

[15] A. M. Ito, Y. Yoshimoto, S. Saito, A. Takayama and H. Nakamura: Physica Scripta **2014** (2014) 014062.

[16] A. Lasa, S. K. Tähtinen and K. Nordlund: EPL (Europhysics Letters) **105** (2014) 25002.

[17] A. Ito *et al.*: Nuclear Fusion **55** (2015) 073013.

[18] C. S. Becquart and C. Domain: Phys. Rev. Lett. **97** (2006) 196402.

[19] L. Chen, Y. Liu, H. Zhou, S. Jin, Y. Zhang and G. Lu: Science China Physics, Mechanics and Astronomy **55** (2012) 614.

[20] Y. Zhou, J. Wang, Q. Hou and A. Deng: Journal of Nuclear Materials **446** (2014) 49.

[21] W. D. Wilson, C. L. Bisson and M. I. Baskes: Phys. Rev. B **24** (1981) 5616.

[22] K. Henriksson, K. Nordlund and J. Keinonen: Nuclear Instruments and Methods in Physics Research Section B: Beam Interactions with Materials and Atoms **244** (2006) 377.

[23] F. Ferroni, K. D. Hammond and B. D. Wirth: Journal of Nuclear Materials **458** (2015) 419.

[24] R. Kobayashi, T. Hattori, T. Tamura and S. Ogata: Journal of Nuclear Materials **463** (2015) 1071.

[25] F. Sefta, K. D. Hammond, N. Juslin and B. D. Wirth: Nuclear Fusion **53** (2013) 073015.

[26] S. Kajita, Y. Tsuji and N. Ohno: Phys. Lett. A **378** (2014) 2533.

[27] S. Kajita, N. Yoshida, N. Ohno and Y. Tsuji: New Journal of Physics **17** (2015) 043038.

[28] K. O. E. Henriksson, K. Nordlund, A. Krasheninnikov and J. Keinonen: Applied Physics Letters **87** (2005) 163113.

[29] C. Becquart and C. Domain: Journal of Nuclear Materials **385** (2009) 223 .

[30] N. Ohno, Y. Hirahata, M. Yamagiwa, S. Kajita, M. Takagi, N. Yoshida, R. Yoshihara, T. Tokunaga and M. Tokitani: Journal of Nuclear Materials **438, Supplement** (2013) S879.

[31] S. Kajita, T. Ishida, H. Dogyun, N. Ohno and T. Yoshida: submitted to Sci. Rep.

[32] T. Novakowski, J. Tripathi and A. Hassanein: Journal of Nuclear Materials **467, Part 1** (2015) 244.

[33] D. L. Turcotte: Journal of Geophysical Research: Solid Earth **91** (1986) 1921.

[34] H. Takayasu, *Fractal (in Japanese)* (Asakura Publishing Co. Ltd., 1986).

[35] J. You, K. Kauhanen and J. Raitala: Earth, Moon, and Planets **71** (1995) 9.

[36] A. Fujiwara, G. Kamimoto and A. Tsukamoto: Icarus **31** (1977) 277.

[37] A. M. Ito *et al.*: Journal of Nuclear Materials **463** (2015) 109.

TABLE I: A summary of tungsten samples analyzed.

Sample No	crystal	Surface temperature	Incident ion energy	He fluence
W1	SC 100	1800 K	55 eV	6×10^{24} m^{-2}
W2	SC 100	1800 K	55 eV	1.8×10^{25} m^{-2}
W3	SC 100	1800 K	55 eV	4.7×10^{25} m^{-2}
W4	PC	1700 K	25 eV	5.3×10^{26} m^{-2}
W5	SC 100	1200 K	73 eV	3×10^{24} m^{-2}
W6	SC 100	1600 K	27 eV	1.5×10^{25} m^{-2}
W7	SC 110	1800 K	55 eV	6×10^{24} m^{-2}
W8	SC 110	1800 K	55 eV	1.8×10^{25} m^{-2}
W9	SC 110	1800 K	55 eV	4.7×10^{25} m^{-2}
W10	SC 100	1550 K	70 eV	6×10^{24} m^{-2}
W11	SC 100	1550 K	70 eV	1.0×10^{25} m^{-2}
W12	SC 100	1550 K	70 eV	1.6×10^{25} m^{-2}

TABLE II: A summary of tantalum samples analyzed.

Sample No	Surface temperature	Incident ion energy	He fluence
Ta1	940 K	63 eV	2.2×10^{26} m^{-2}
Ta2	1090 K	46 eV	8.4×10^{25} m^{-2}
Ta3	1250 K	70 eV	4.5×10^{25} m^{-2}
Ta4	1420 K	77 eV	1.2×10^{26} m^{-2}
Ta5	1480 K	95 eV	1.1×10^{26} m^{-2}

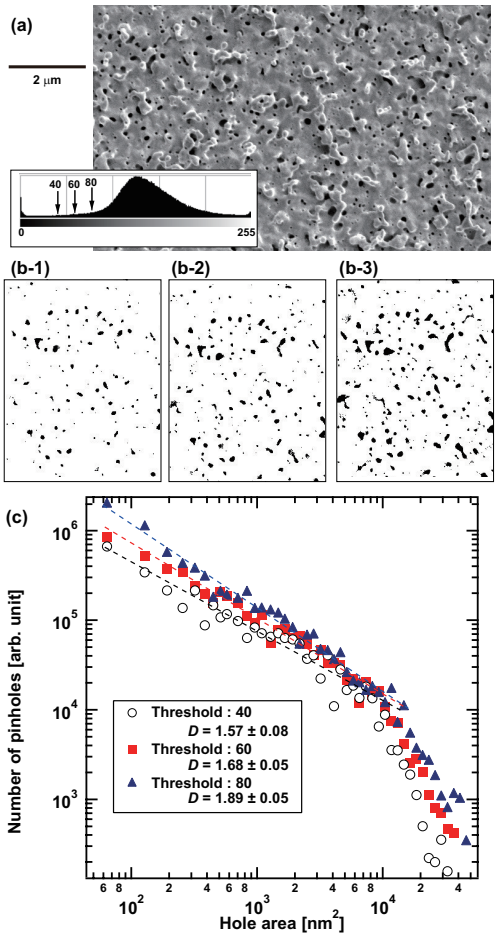

FIG. 1: (a) An SEM micrographs of the He irradiated sample (W2) with the contrast profile, (b) three digitized images with the threshold level of 40, 60 and 80, and (c) the cumulative number density distribution of pinholes as a function of the hole area.

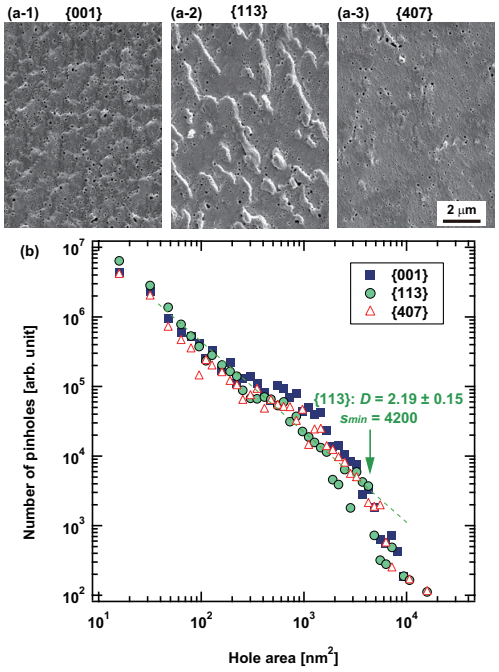

FIG. 2: (a-1)-(a-3) SEM micrographs of the sample W4 at different crystal orientation measured by OIM method and (b) the cumulative number density distribution of pinholes as a function of the hole area.

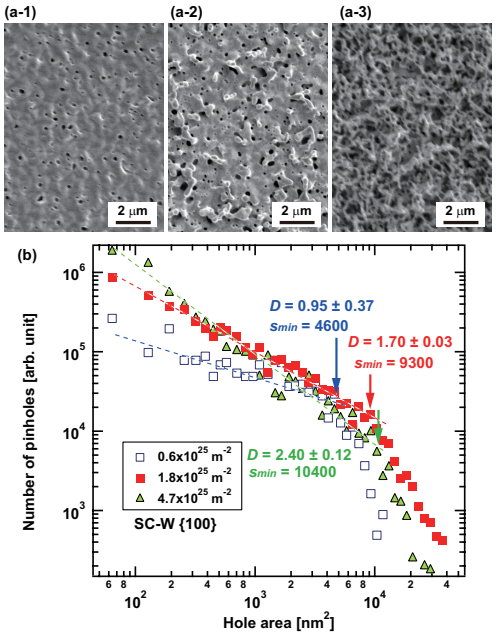

FIG. 3: (a-1)-(a-3) SEM micrographs of W1-W3 and (b) the relations between the cumulative density of pinholes and the pinhole area.

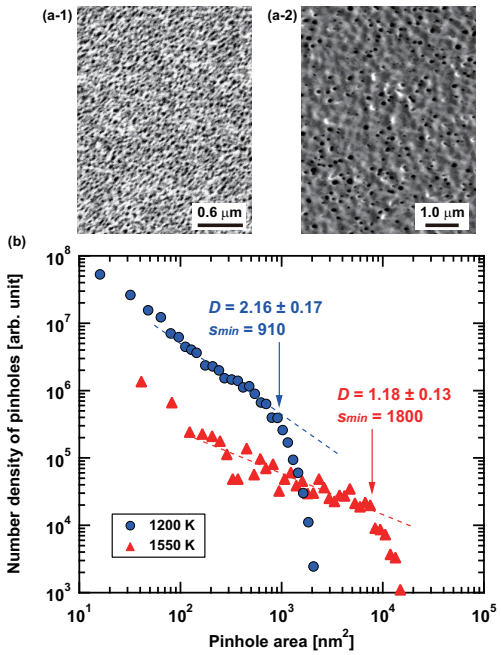

FIG. 4: (a-1)-(a-3) SEM micrographs of W1 and W5 and (b) the relations between the cumulative density of pinholes and the pinhole area.

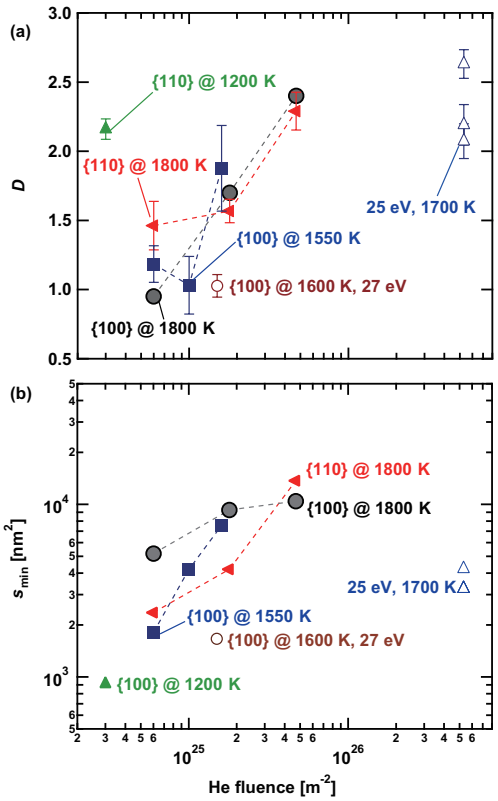

FIG. 5: Estimated (a) D and (b) $s_{\min}$ as a function of the He fluence.

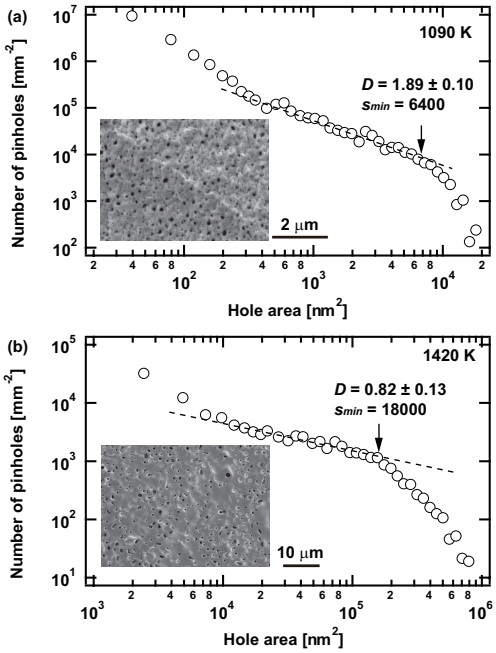

FIG. 6: Cumulative number density distribution of pinholes on (a) Ta2 and (b) Ta4 as a function of the pinhole size.

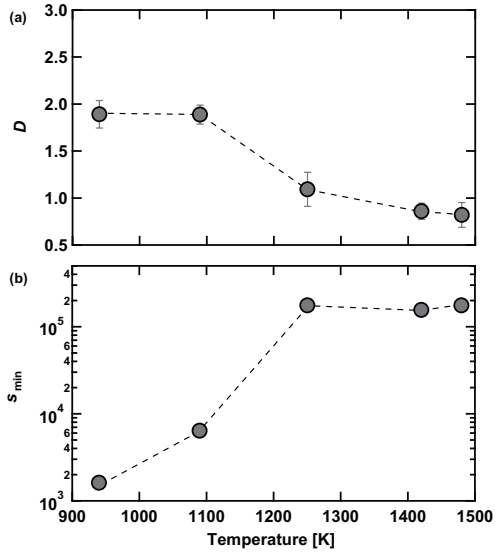

FIG. 7: Temperature dependences of (a) D and (b) $s_{\min}$ for tantalum exposed to He plasmas.

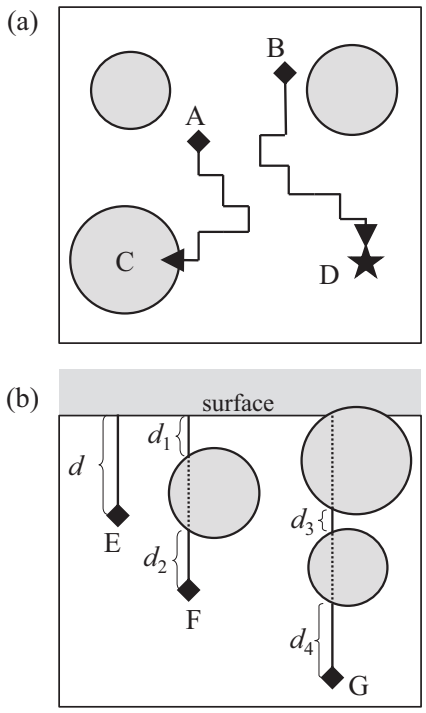

FIG. 8: (a) A schematic of random walk processes in the models and (b) a schematic illustrating the injection process in the second model. The gray circles indicate the existing bubbles. The rhombuses indicate the start positions of random walks of helium atoms.

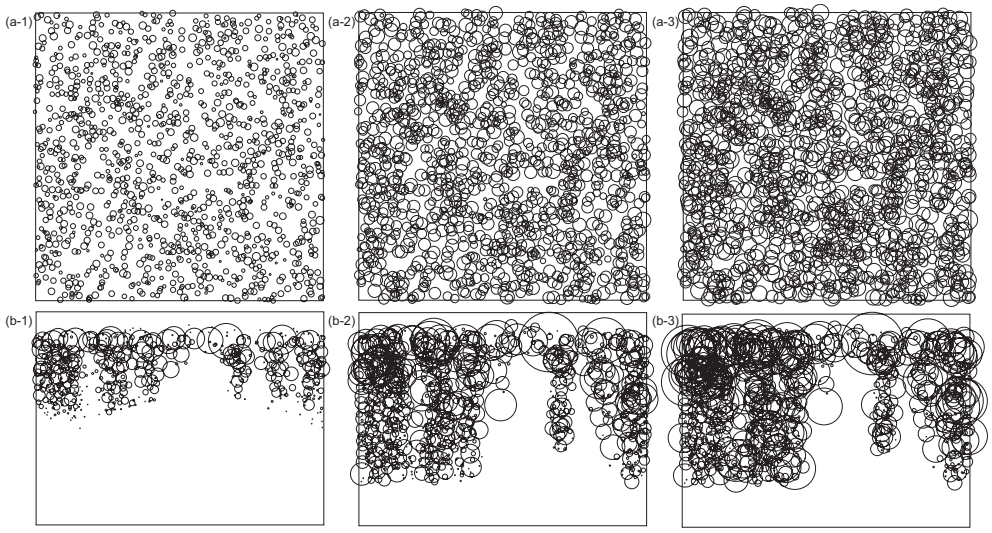

FIG. 9: The spatial distributions of helium bubbles in (a-1)-(a-3) the first model and (b-1)-(b-3) the second model. The number N_{step} is (a-1)(b-1) 10^5, (a-2)(b-2) 4×10^5, and (a-3)(b-3) 7×10^5.

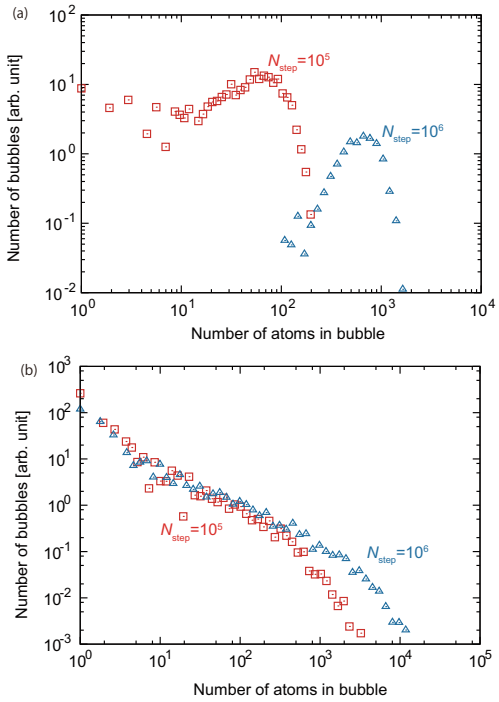

FIG. 10: The cumulative number density of helium bubbles as a function of the number of atoms in a bubble in (a) the first model and (b) the second model.